Sensor and Simulation Notes

Note 474

3 June 2003

Numerical Analysis of the Impulse-Radiating Antenna

Kangwook Kim and Waymond R. Scott, Jr.

School of Electrical and Computer Engineering

Georgia Institute of Technology

ABSTRACT

Two reflector-type impulse-radiating antennas with focal length to diameter ratios of 0.25 and 0.5 are numerically analyzed. The numerical model is developed using the method of moments code in the EIGER code suite. The performance of the numerical model is validated by comparing the radiated field measured on boresight and the reflected voltage measured in the transmission line with the results from the numerical model. Using the numerical model, the contribution of each part of the antenna to the radiated field and the reflected voltage is identified. The reflected voltage waveform in the transmission line and the electric field waveforms both in the near- and far-zones are presented. The impulse and prepulse amplitudes, spot sizes, and power budgets are also presented.

I. Introduction

A number of applications require radiation of a short pulse to detect and identify targets [1–5]. One candidate antenna for such applications is the reflector-type impulse-radiating antenna (IRA) [6–10]. The reflector-type IRA can radiate a short pulse that is highly directive. The antenna is also efficient because it can be made to radiate a large portion of the input energy by matching the characteristic impedance of the transmission line to that of the transverse electromagnetic (TEM) feed structure and by appropriately terminating the TEM feed structure at the reflector.

A simple analytical model that gives the radiated fields on boresight has already been developed by Baum et al. [9–13]. The model has been extended to work off boresight and in the near zone in [14]. However, neither of these models can predict tail waveforms, power budgets, etc. These characteristics can easily be obtained by modeling the IRAs numerically.

Two IRAs are numerically modeled and analyzed; one with a focal length to diameter ratio (F/D) of 0.25 (flat IRA) and one with a F/D of 0.5 (tall IRA). The performance of the numerical model is validated by a set of measurements. The numerical model enables one to obtain various characteristics of the IRAs, such as far- and near-field waveforms, illuminated spot sizes, and power budget. The numerical model has been developed using the method of moments (MoM) code in the electromagnetic interactions generalized (EIGER) code suite [15–17].

II. Modeling of Impulse-Radiating Antennas

Let us consider the IRAs shown in Fig. 1. Each IRA has two pairs of conical-coplanar-plate TEM feed arms, which are placed perpendicular to each other. The TEM feed arms have a conical geometry within a sphere of radius L centered at the drive point, where a spherical TEM wave launched at the drive point propagates outwardly without disturbance. The angles associated with the TEM feed arms are chosen such that the characteristic impedance of each pair of the arms is 400Ω in the undisturbed section. Outside the spherical region of radius L, the TEM feed arms are linearly tapered and connected to the reflector

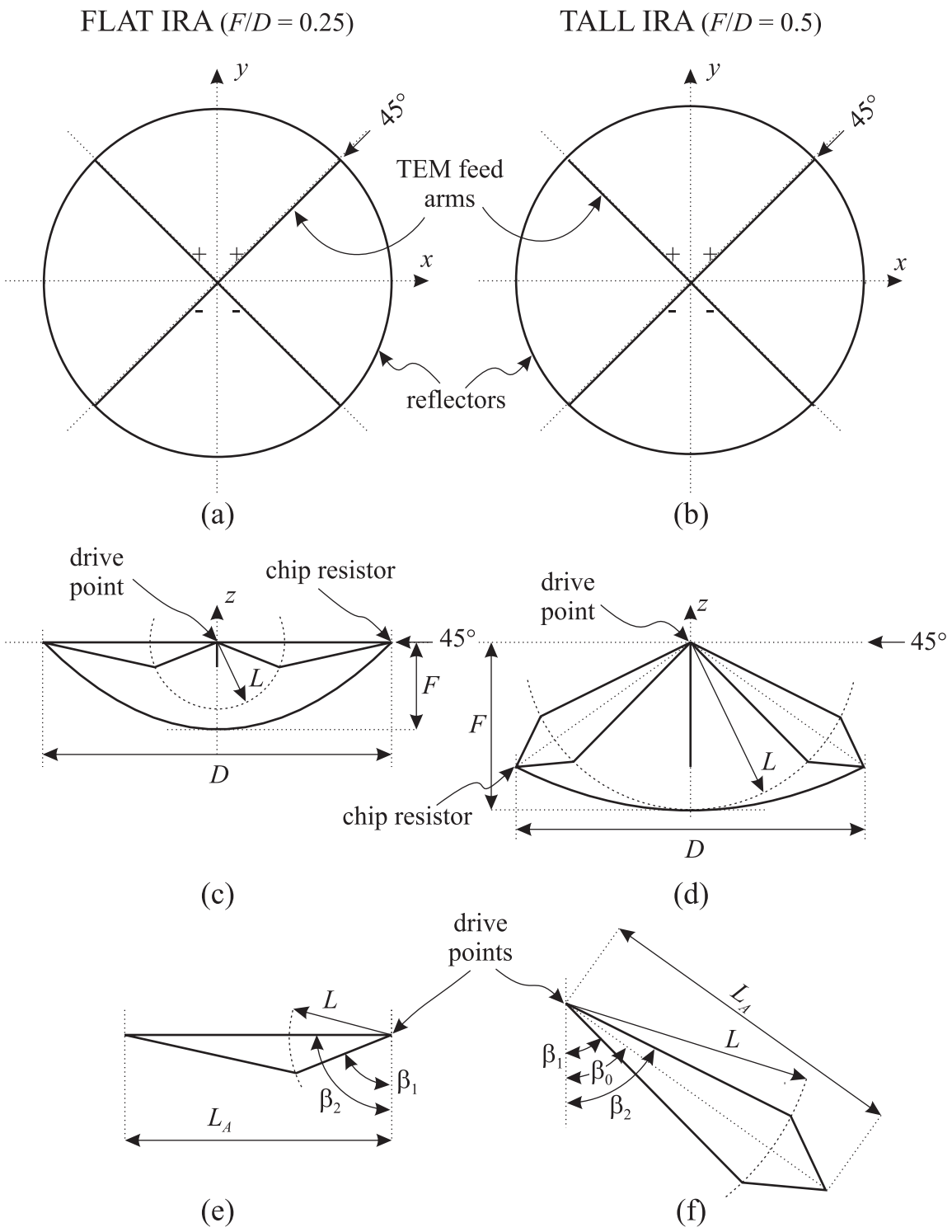

Fig. 1. Comparison of the two IRA geometries. (a), (b) Top view. (c), (d) Side view. (e), (f) Feed arm dimensions.

TABLE I

DIMENSIONS OF THE IRAS.

	F/D	L/D	β_0	β_1	β_2
Flat IRA	0.25	0.19		73.87°	90°
Tall IRA	0.5	0.5	53.01°	46.88°	59.94°

through 200Ω chip resistors, which are used as low frequency matching circuits.

The IRA is excited at the drive point. Each pair of arms can be excited independently to radiate two polarizations or excited in parallel to lower the characteristic impedance of the arm structure [18]. In this paper, the arms in the positive-y half-space are connected together, and the arms in the negative-y half-space are connected together at the drive point. The resulting characteristic impedance of the TEM feed structure is 200Ω. The dimensions are summarized in Table I for the two IRAs.

The IRA has redundancies in the geometry. By eliminating these redundancies, the efficiency of the numerical model can be significantly improved. Note that one pair of TEM feed arms is placed in the symmetry plane of the other pair of TEM feed arms, where the tangential electric field is zero. Thus, the field generated by the first pair is independent of the existence of the second pair, and the fields generated by the two pairs are simply the orthogonal versions of each other. Thus, the geometry of the IRA with one pair of TEM feed arms can produce enough data to predict the response of the IRA with two pairs of TEM feed arms. The 2-arm IRA still has reflection symmetry. This allows one to replace half of the 2-arm IRA geometry with a perfect electric conductor (PEC) plane placed orthogonal to the TEM feed arms. The PEC plane mirrors the remaining geometry. Thus, only half of the reflector and one TEM feed arm need to be included in the numerical model [1].

A MATLAB® program was written to generate the mesh for the numerical model. Fig. 2 shows the meshes generated for the two IRAs. The mesh contains one TEM feed arm

[1]Note that half of the resulting geometry can be replaced with a perfect magnetic conductor (PMC) plane placed at the TEM feed arms. This would have allowed one to include only one TEM feed arm and a quarter of the reflector in the model; however, a PMC plane is not supported by EIGER [19].

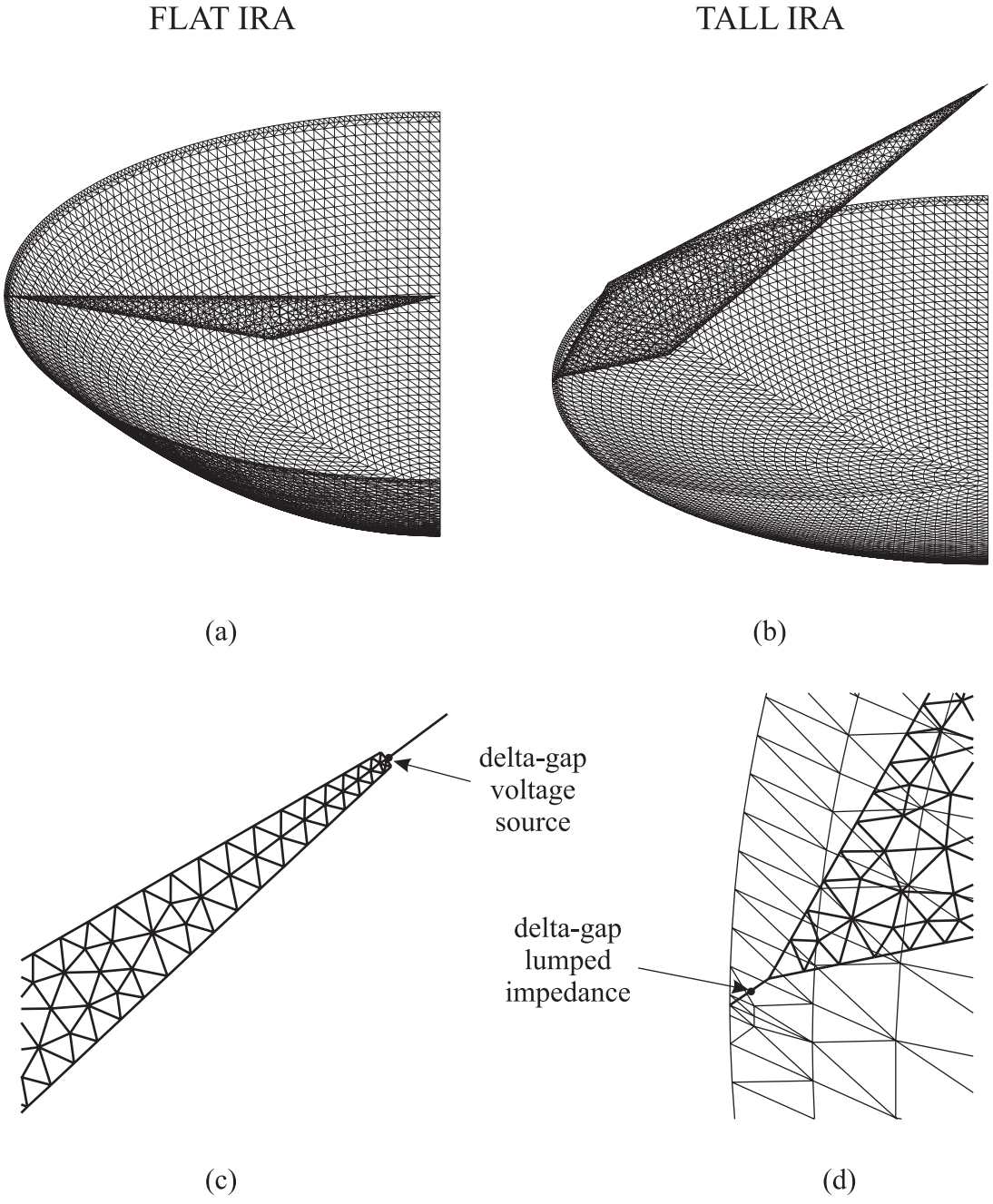

Fig. 2. (a), (b) Meshes used for the numerical model of the IRAs. (c) Detail view of the mesh around the apex of the tall IRA. (d) Detail view of the mesh around the arm termination of the tall IRA. The locations of the delta-gap elements are marked by dots.

and half of the reflector for each IRA. The mesh for the IRA with $F/D = 0.25$ is composed of 8930 triangle elements and 3 wire elements, and the mesh for the IRA with $F/D = 0.5$ is composed of 9252 triangle elements and 3 wire elements. The triangle elements are used to mesh the PEC surfaces, e.g., the TEM feed arm and the reflector, and the wire elements are used to mesh the lumped elements, e.g., the drive point and the chip resistor. The drive point is modeled using a delta-gap voltage source. The chip resistor is modeled using a 200Ω delta-gap lumped impedance model. Note that the mesh density is increased around the edges of the reflector and the TEM feed arm to represent fast varying currents at the edges better. The mesh is further refined in the TEM feed arm because the current density is high in the arm.

The mesh is excited by the delta-gap voltage source. The electric field integral equation (EFIE) with linear basis functions is used to solve for the mesh currents. The EIGER physics solver (EIGER Solve) is executed in parallel using the message passing interface (MPI) protocol to produce the mesh currents. The calculation is conducted at 160 frequency points from 125MHz ($D/\lambda = 0.128$) to 20GHz ($D/\lambda = 20.4$) with 125MHz increments on the Beowulf cluster at the Electromagnetics/Acoustics Laboratory at the Georgia Institute of Technology.[2] The run times for the mesh current calculation were approximately 91.3 hours for the IRA with $F/D = 0.25$ and 99.2 hours for the IRA with $F/D = 0.5$ using 32 computer nodes; each node is equipped with an AMD Athlon$^{\text{TM}}$ 2200+ processor.

The fields and the input impedance are obtained by running EIGER Analyze, which is the EIGER physics solver for secondary quantities. The quantities generated by the EIGER physics solvers are the responses of the IRA with one TEM feed arm and half of the reflector attached to the PEC ground plane. The responses of the 2-arm IRA with one pair of TEM feed arm and a full reflector without the PEC ground plane can be obtained through a simple algebraic manipulation of the quantities generated by the numerical model, e.g., halving the fields, halving the currents, and doubling the input impedance. The responses of the full

[2]Note that the upper frequency limit was chosen because of computer run time considerations, not limits on the IRA. The chosen upper frequency limit gives us reasonable run times while giving us enough frequency content to see essentially all of the interesting interactions in the antennas. This upper frequency limit sets the minimum pulse parameters in the later graphs.

IRA whose geometry is shown in Fig. 1 are then obtained through a simple manipulation of the responses of the 2-arm IRA. The currents and fields of the full IRA are obtained by first rotating the 2-arm IRA by -45° and $+45^\circ$ and then adding the currents and fields of the rotated 2-arm IRAs vectorially. The input impedance of the full IRA is obtained by halving the input impedance of the 2-arm IRA [20].

The responses in the frequency domain are transformed into the time domain for a voltage pulse incident in a transmission line. The input pulses considered in this paper are step-like, Gaussian, and differentiated Gaussian. These functions are defined as follows:

$$\text{Step-like:} \quad V(t) = V_0 \left\{ \frac{1}{2} + \frac{1}{2} \operatorname{erf} \left(k_1 \frac{t}{t_{10\text{-}90\%}} \right) \right\}, \tag{1}$$

$$k_1 = 2 \operatorname{erf}^{-1}(0.8) \simeq 1.8124,$$

$$\text{Gaussian:} \quad V(t) = V_0 e^{-\ln 16 (t/t_{FWHM})^2}, \tag{2}$$

$$\text{Differentiated Gaussian:} \quad V(t) = V_0 \frac{t}{t_{P\text{-}P}} e^{0.5 - 2(t/t_{P\text{-}P})^2}. \tag{3}$$

Here, $\operatorname{erf}(t)$ is the error function [21], and the pulse parameters $t_{10\text{-}90\%}$, t_{FWHM}, and $t_{P\text{-}P}$ are the 10% – 90% rise time of the step-like pulse, the full-width half-maximum of the Gaussian pulse, and the peak-to-peak interval of the differentiated Gaussian pulse, respectively. The time domain waveforms of these pulses and the corresponding frequency spectrums are shown in Fig. 3, where the half-maximum frequency for the Gaussian pulse is

$$f_{1/2} = \frac{\ln 4}{\pi t_{FWHM}}, \tag{4}$$

and the peak frequency for the differentiated Gaussian pulse is

$$f_{PK} = \frac{1}{\pi t_{P\text{-}P}}. \tag{5}$$

III. Validation of the Numerical Models

To validate the performance of the numerical model, the radiated field on boresight and the reflected voltage in the transmission line are measured and compared with those

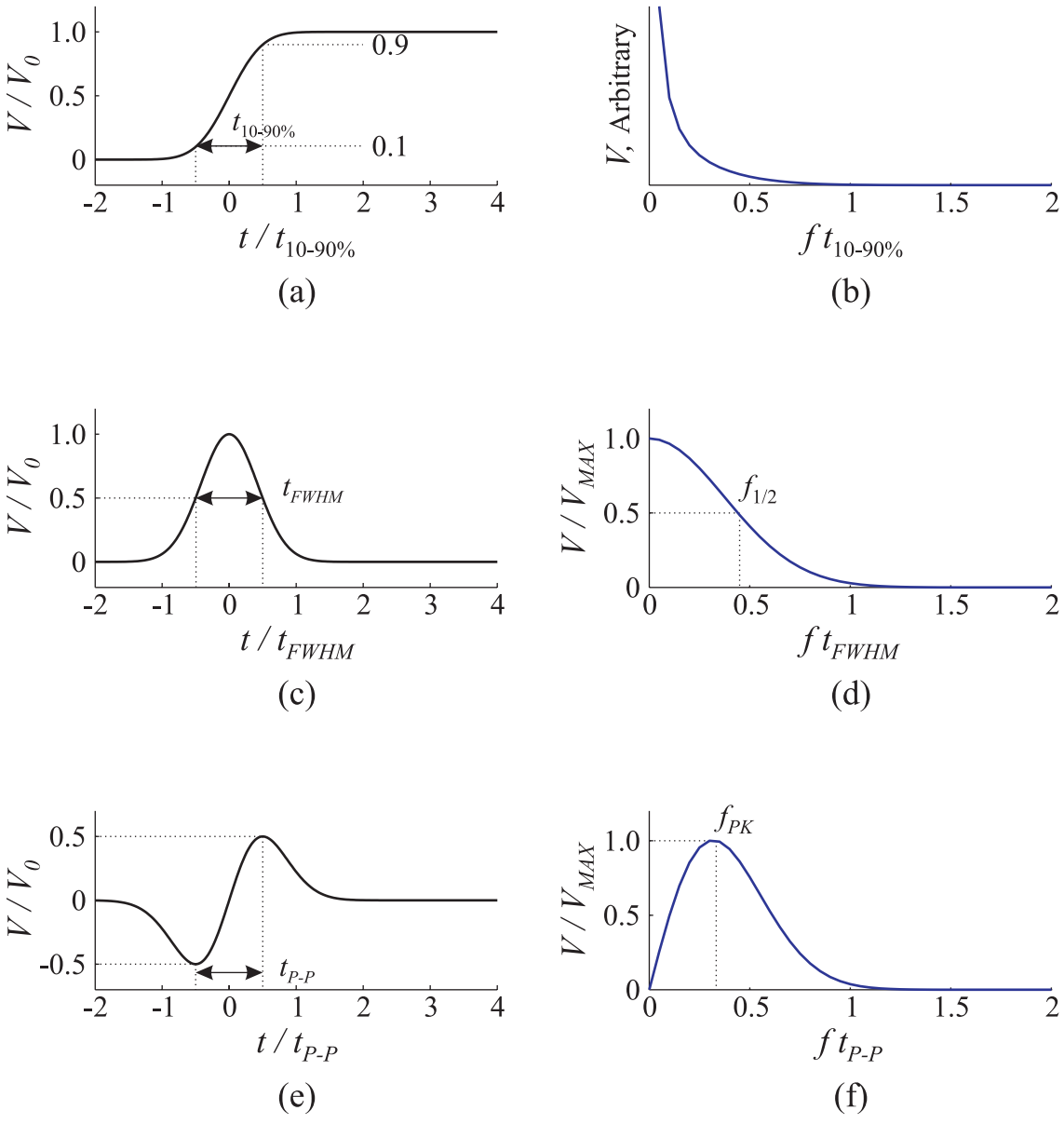

Fig. 3. Input pulses. The graphs in the left column are the time domain waveforms for (a) a step-like pulse, (c) a Gaussian pulse, (e) a differentiated Gaussian pulse. The graphs in the right column are the corresponding frequency spectrums for (b) the step-like pulse, (d) the Gaussian pulse, and (f) the differentiated Gaussian pulse.

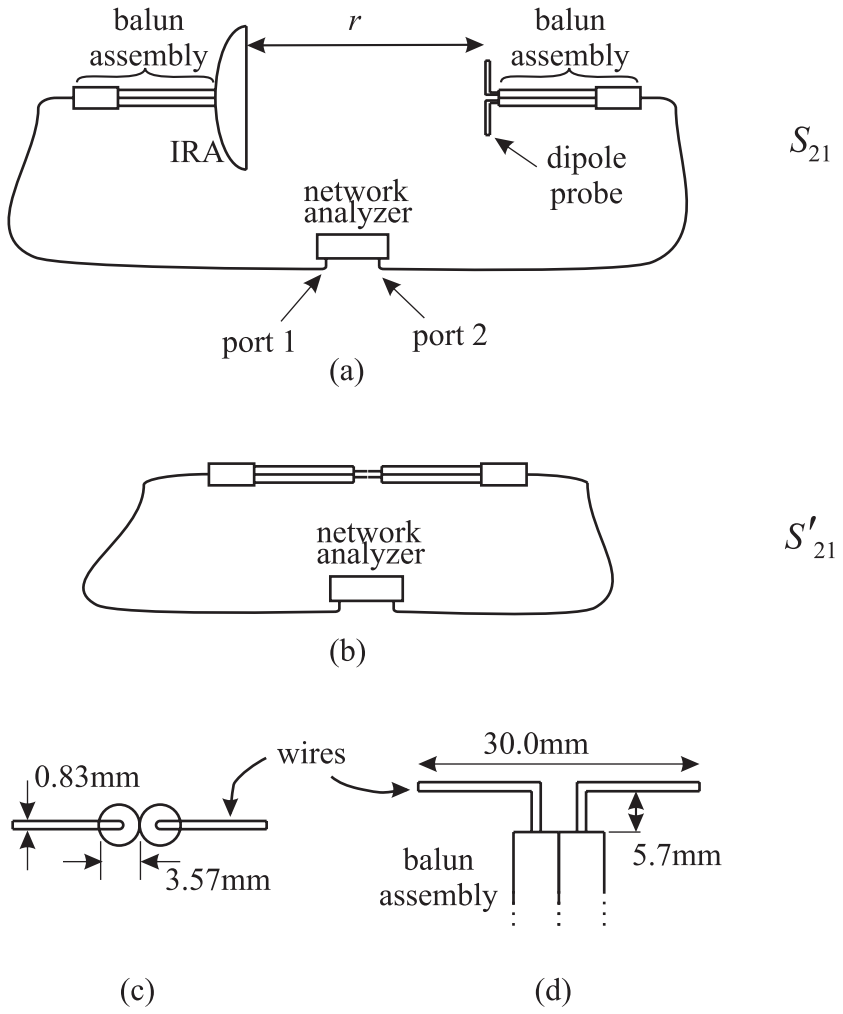

Fig. 4. Measurement setup for the radiated field of the IRA. (a) Measurement of the radiated field, (b) Measurement of thru, which is used to compensate for the delay and attenuation along the balun assemblies and coaxial cables. (c) Top view of the dipole probe. (d) Side view of the dipole probe.

calculated from the numerical model. The setup for the radiated field measurement is schematically shown in Fig. 4. The IRA used in the measurement is a slightly modified version of the antennas used in [1]. The flat IRA ($D = 30.6$cm) and a small dipole probe are connected to a network analyzer through balun assemblies and coaxial cables. The geometry of the dipole probe is shown in Fig. 4 (c) and (d).

The diagram of the balun assembly is schematically drawn in Fig. 5. The balun assembly consists of a Picosecond Pulse Labs Model 5315A Balun [22] and a pair of 50Ω semi-rigid coaxial cables. The coaxial cables are connected to the output ports of the balun,

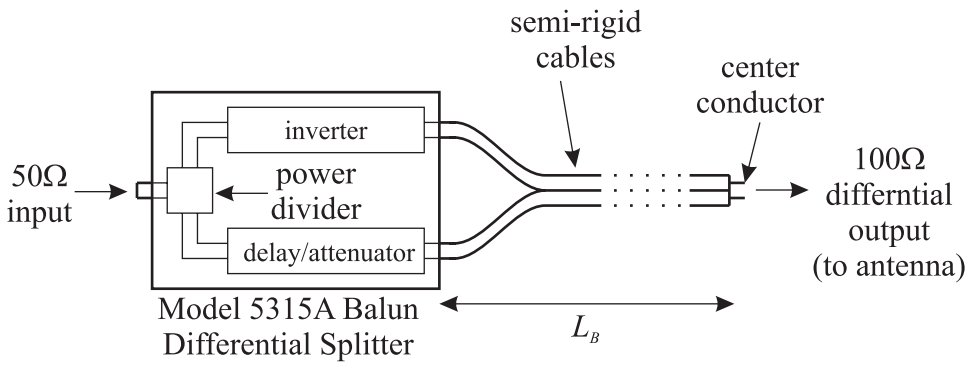

Fig. 5. Schematic of the balun assembly. A Picosecond Pulse Labs Model 5315A Balun is connected to two semi-rigid 50Ω coaxial cables. ($L_B \simeq 60$cm)

which have opposite polarities. The outer conductors of the cables are connected together to form a 100Ω balanced transmission line. The cable pair is about 60cm long. This length creates a time window of about 5.8nsec in which no multiple reflections exist between the antenna and the balun because it takes that amount of time for a signal to make a round trip inside the cable pair.

The radiated field of the IRA is received by a small dipole probe, which is placed r away from the IRA. The network analyzer measures the frequency response of the system (S_{21}) by sweeping frequency points from 63MHz to 10.143GHz with 6.3MHz increments. This measurement includes the delay and attenuation in the balun assemblies and cables. To compensate S_{21} for the delay and attenuation, a simple calibration procedure is applied. First, the IRA and the dipole probe are removed from the balun assemblies, and then the balun assemblies are connected back to back. The data measured from this configuration (S'_{21}) contains the same amount of delay and attenuation as S_{21} does. Thus, by dividing S'_{21} into S_{21}, we can remove the delay and attenuation and obtain the transmission coefficient ($T = S_{21}/S'_{21}$) from the IRA to the dipole probe. This transmission coefficient is then transformed into the time domain for an input pulse incident in a 100Ω transmission line to the IRA. The result is the time-domain waveform of the voltage across the dipole probe, which is connected to a 100Ω transmission line. The waveform still includes unwanted signals, such as reflections from the measurement equipment, reflections from the ground, and multiple reflections between the antenna and the balun. These unwanted signals are

removed by gating in the time domain.

The transmission coefficient is also obtained from the numerical model. First, the electric field of the IRA is obtained from the numerical model. Next, the dipole is also numerically modeled. In the numerical model, the dipole probe is loaded with a 100Ω lumped resistor at the center to simulate the 100Ω transmission line and illuminated by a planewave. Then, the effective height of the dipole probe is calculated as:

$$\bar{h}_d(\omega) = \frac{I_L(\omega)R}{E_0}\hat{y}, \tag{6}$$

where $I_L(\omega)$ is the current through the load ($R = 100\Omega$), E_0 is the amplitude of the plane wave illuminating the dipole. Finally, the electric field of the IRA, the effective height of the dipole, and the input pulse incident in a 100Ω transmission line are convolved to give a time-domain waveform of the voltage across the dipole probe.

The resulting waveform obtained from the numerical model is compared with the measured waveform in Fig. 6. The figure shows the waveforms measured at seven distances ranging from $r/D = 6.97$ to $r/D = 24.9$ for three input pulses: a step-like pulse with $t_{10\text{-}90\%}/\tau_a = 0.15$, a Gaussian pulse with $t_{FWHM}/\tau_a = 0.15$, and a differentiated pulse with $t_{P\text{-}P}/\tau_a = 0.15$. For each input pulse, the waveform is plotted as a function of retarded time, $t_r = t - r/c$, and vertically displaced according to the distance between the IRA and the dipole probe. The horizontal axis is normalized by $\tau_a = D/c$, which is the time required by light to travel across the reflector diameter. As shown, the measured waveforms are in good agreement with the waveforms obtained from the numerical model. The slight mismatch in the amplitude is believed to be from the error in the simple calibration procedure. The measurement for S'_{21} includes a discontinuity at the junction between the two balun assemblies. This discontinuity causes a reduction in S'_{21}, which in turn leads to an increase in the transmission coefficient, and therefore results in an increased waveform.

The performance of the numerical model is also validated in terms of the reflected voltage in the transmission line. Fig. 7 (a) shows the setup for the reflected voltage measurement. The network analyzer sees the reflection from the IRA through the cable and the balun assembly, which can be considered as a two-port network. Thus, the reflection

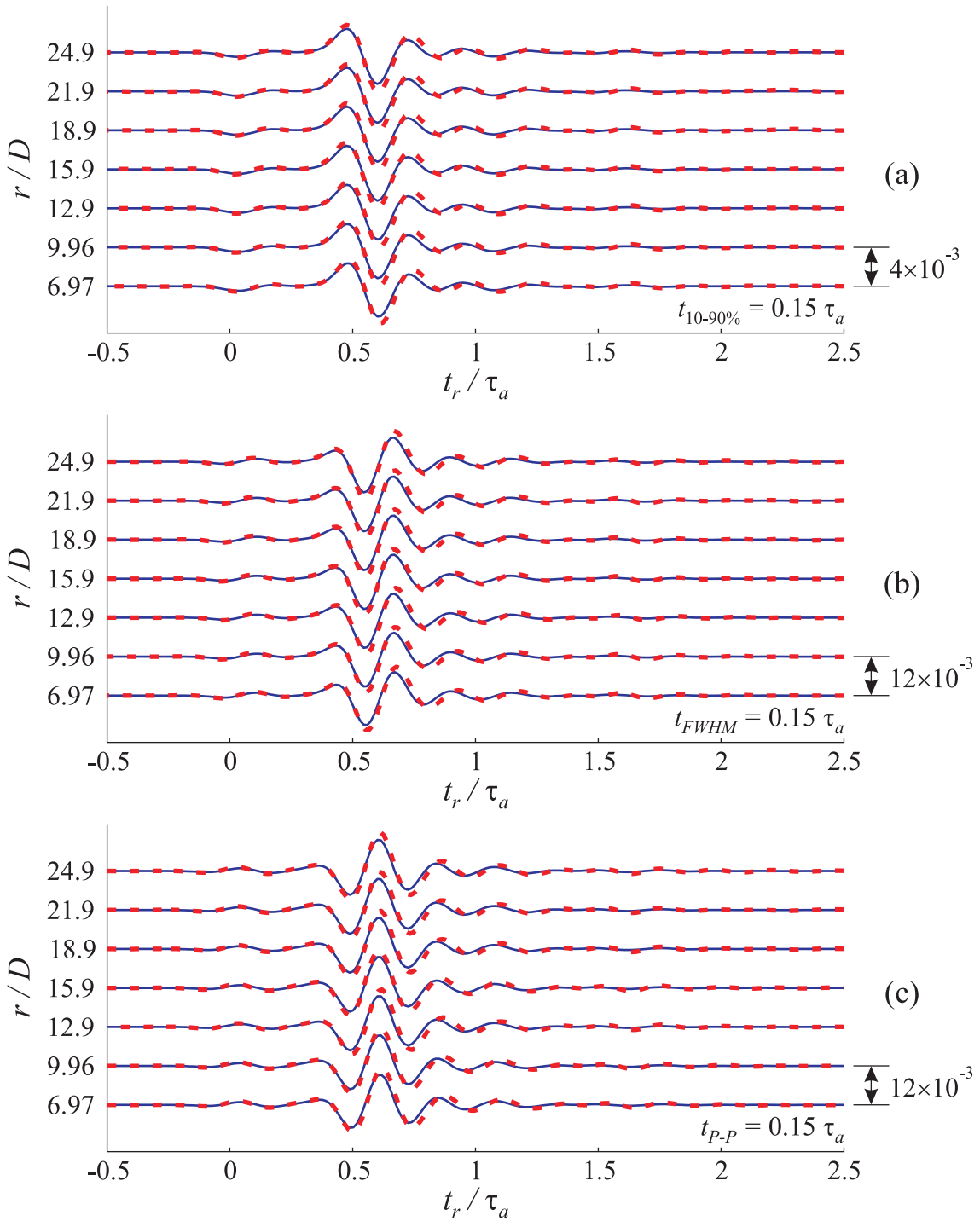

Fig. 6. Voltages across the dipole probe as functions of time for (a) a step-like voltage pulse with $t_{10\text{-}90\%}/\tau_a = 0.15$, (b) a Gaussian voltage pulse with $t_{FWHM}/\tau_a = 0.15$, and (c) a differentiated Gaussian voltage pulse with $t_{P\text{-}P}/\tau_a = 0.15$ incident in a 100Ω transmission line. The solid lines are voltages across the dipole probe obtained numerically, and the dotted lines are those measured. Each waveform is normalized by V_0 and vertically displaced according the distance between the IRA and the dipole probe.

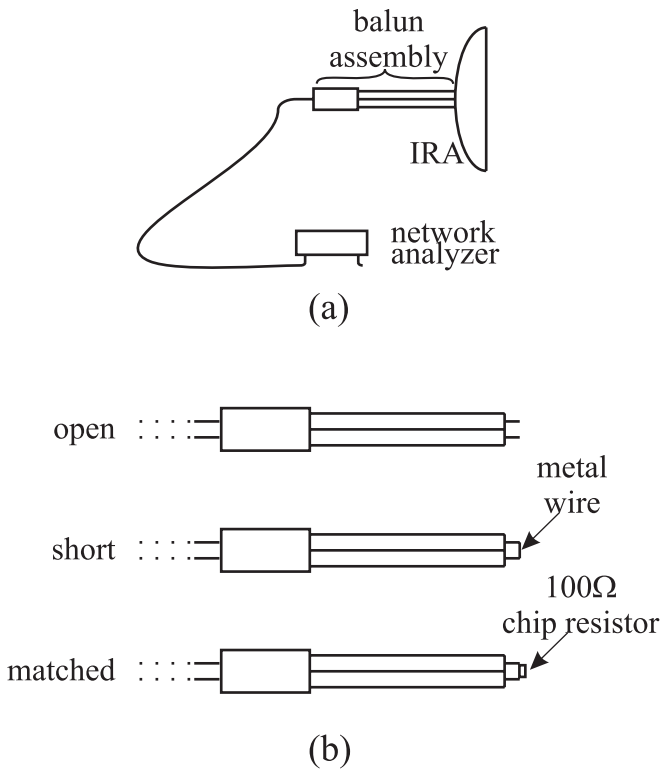

Fig. 7. Measurement setup for the reflection from the IRA. (a) Measurement of the reflection through a two-port network (balun assembly and cable). (b) Measurement of the three standards through the two-port network.

measured by the network analyzer may be expressed as [23]:

$$\Gamma_{ANA} = S_{11}^B + \frac{S_{12}^B S_{21}^B \Gamma_{IRA}}{1 - S_{22}^B \Gamma_{IRA}}, \tag{7}$$

where S_{11}^B, S_{22}^B, and $S_{12}^B S_{21}^B$ are the scattering parameters of the two-port network, and Γ_{IRA} is the reflection from the IRA seen from a 100Ω transmission line. The three S-parameters can be identified by measuring three known standards, e.g., open, short, and match. Fig. 7 (b) shows the measurement of these three standards. The balun assembly is simply left open for the open and shorted by a piece of metal wire for the short. The balun is terminated with a 100Ω chip resistor for the match. Once the S-parameters are obtained, the reflection from the IRA (Γ_{IRA}) is calculated by inverting Eq. (7). The reflection is measured at 1601 frequency points from 50MHz to 20.05GHz with 12.5MHz increments. Because the TEM feed structure of the IRA is designed to be connected to a 200Ω transmission line, the reflection in a 200Ω transmission line is more appropriate. The reflection in the 200Ω transmission

line can be obtained by a simple conversion:

$$\Gamma = \frac{(Z_1 - Z_0) + (Z_1 + Z_0)\Gamma_{IRA}}{(Z_1 + Z_0) + (Z_1 - Z_0)\Gamma_{IRA}}, \tag{8}$$

where $Z_1 = 100\Omega$ is the characteristic impedance at the output of the balun assembly, and $Z_0 = 200\Omega$ is the characteristic impedances of the matched transmission line. The result is then transformed into the time domain for an input pulse incident in the 200Ω transmission line.

The reflection from the IRA in a 200Ω transmission line is also obtained from the numerical model. First, the input impedance calculated from the numerical model is converted to the reflection coefficient seen by the 200Ω transmission line. Then, the reflection coefficient is convolved with an input pulse incident in the transmission line to give the reflected voltage waveform in the time domain.

The resulting waveform obtained from the numerical model is compared with the measured waveform in Fig. 8. The figure shows the reflected voltage in a 200Ω transmission line as a function of time for three input pulses: a step-like pulse with $t_{10\text{-}90\%}/\tau_a = 0.075$, a Gaussian pulse with $t_{FWHM}/\tau_a = 0.075$, and a differentiated pulse with $t_{P\text{-}P}/\tau_a = 0.075$. The solid lines represent the waveforms obtained numerically, and the dotted lines represent those measured. Note that the amplitudes of the waveforms are small. This means that the IRA is well matched to the 200Ω transmission line. The largest reflection occurs at $t/\tau_a \simeq 0$, which comes from the drive point. The drive point in the experimental model is the junction between the balun assembly and the TEM feed arms. This junction is not perfect in the experimental model. The reflection from the junction is simulated in the numerical model by placing a small parallel capacitance (0.065pF) at the junction.

As seen in the figure, the measured waveforms are in good agreement with the waveforms obtained from the numerical model. The results in Fig. 8 (a) are seen to differ over the time interval $0 < t/\tau_a < 0.5$. During this time interval, the reflection comes from the undisturbed section of the TEM feed arms. The reason for this reflection is that the numerical model is not accurately predicting the characteristic impedance of the undisturbed section of the TEM feed arms. The amplitude of the reflection is approximately $0.025V_0$, which is equivalent to the reflection from a 190Ω load. Thus, the numerical model underestimates the

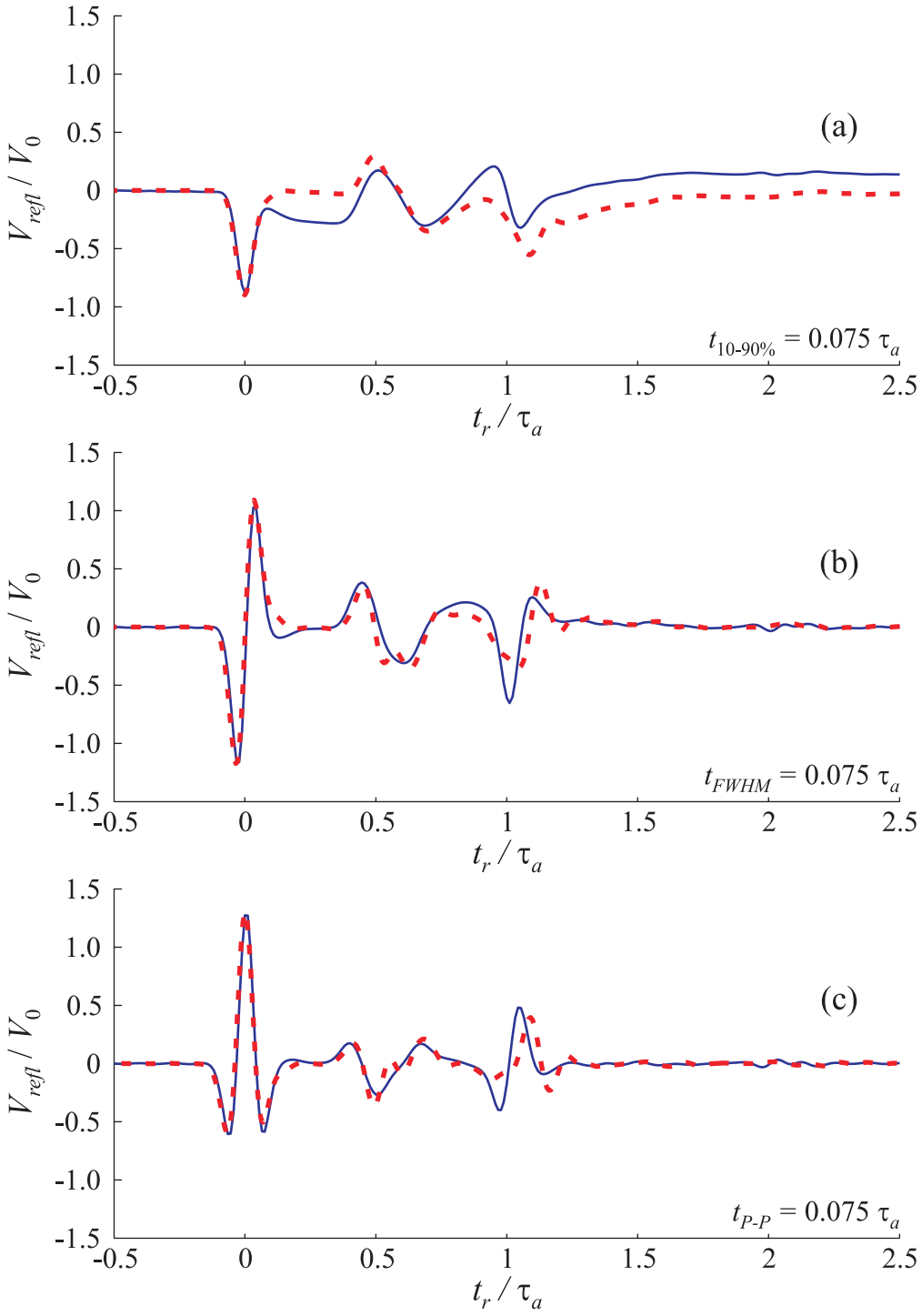

Fig. 8. Reflected voltages in a 200Ω transmission line as functions of time. The solid lines represent those obtained numerically and the dotted lines represent those measured. The antenna is excited by (a) a step-like voltage pulse with $t_{10\text{-}90\%}/\tau_a = 0.075$, (b) a Gaussian voltage pulse with $t_{FWHM}/\tau_a = 0.075$, and (c) a differentiated Gaussian voltage pulse with $t_{P\text{-}P}/\tau_a = 0.075$ incident in the transmission line.

characteristic impedance of the undisturbed section by approximately 5%. In Fig. 8 (a) – (c), the results are seen to differ at $t/\tau_a \simeq 1$, which are the reflections from the matching circuit. This is believed to be from the inaccuracy in the model for the matching circuit. As shown in Fig. 6, these discrepancies do not seem to degrade the performance of the numerical model in predicting the radiated fields.

IV. Analysis of the Impulse-Radiating Antenna

The numerical model was validated in the previous section. In this section, the IRAs with $F/D = 0.25$ and $F/D = 0.5$ are analyzed using the numerical model. The antenna is excited by an input voltage pulse incident in a 200Ω transmission line, which is matched to the characteristic impedance of the TEM feed structure.

In Fig. 9, the radiated fields predicted by the numerical model are compared as functions of time with those predicted by Baum et al.'s analytical model [9, 24]. The waveforms are in good agreement, particularly when the simplicity of the analytical model is considered. The tail waveforms, which are not included in the simple analytical model, mainly result from the multiple reflections between the TEM feed arms and the reflector. The prepulse waveform is distorted near the impulse because of the disturbance from the TEM feed arm termination.

These deviations from the simple analytical model can be understood more clearly by conducting a simple wave path analysis. In Fig. 10, the radiated fields on boresight of the IRAs are plotted as functions of time for a step-like pulse with $t_{10\text{-}90\%}/\tau_a = 0.075$ and a Gaussian pulse with $t_{FWHM}/\tau_a = 0.075$. The beginning of the direct, spherical radiation from the TEM feed arms (prepulse) is marked by **A**. The wave launched at the drive point is spherically guided by the TEM feed arms. Thus, the waveform is a replica of the signal at the drive point until the guided wave is disturbed by the linear taper after the radial distance L. The beginning of the signal from the tapered section is marked by **T**. The wave guided toward the reflector is reflected back and forms a planar aperture. Because the reflector is a part of a paraboloid, and the drive point is located at the focal point of the paraboloid, the

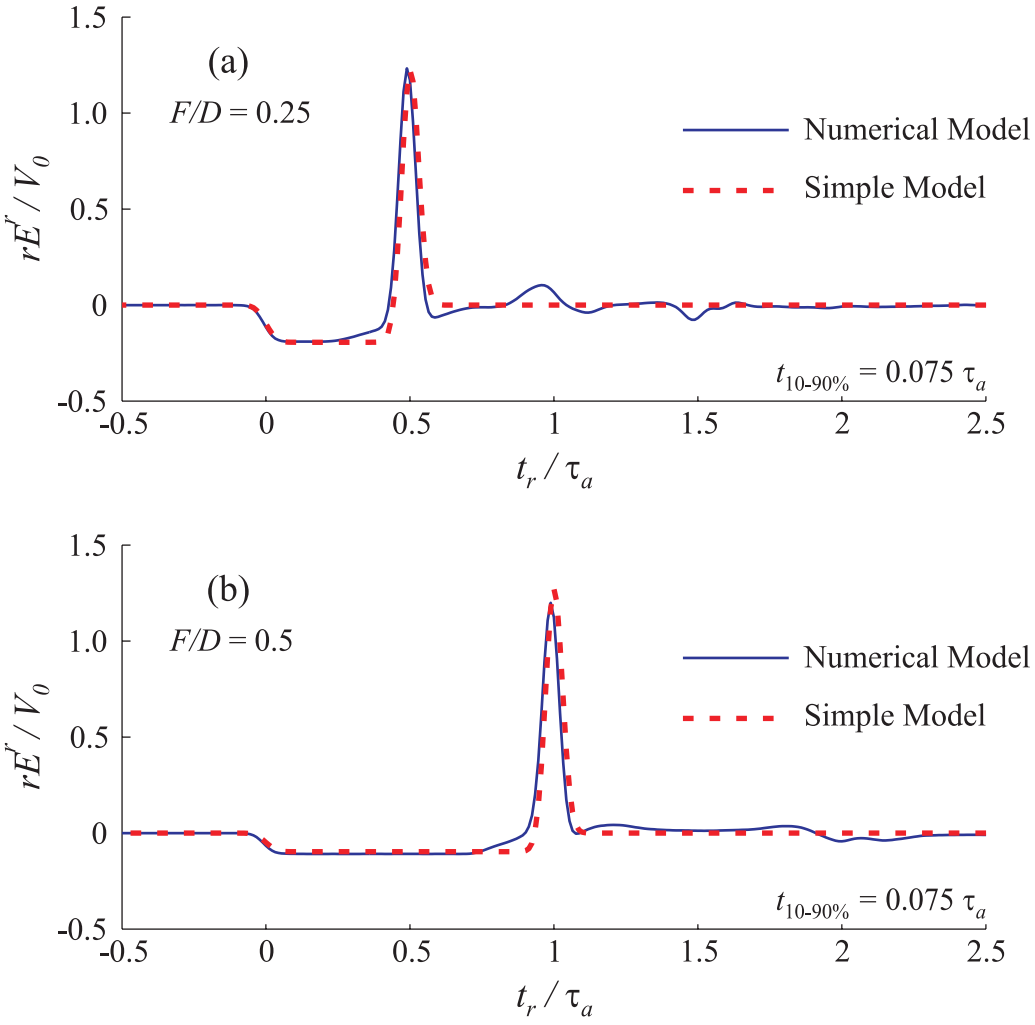

Fig. 9. Boresight waveforms predicted by the numerical model (solid line) and the simple model (dotted line) when the input pulse is a step-like pulse with $t_{10\text{-}90\%}/\tau_a = 0.075$. The focal length to diameter ratios ($F/D's$) for the antenna are (a) 0.25 and (b) 0.5.

field at each point of the aperture has the same time-dependence. For this type of aperture, the radiation is a derivative of the aperture field. This radiation (impulse) is marked by **D** in the figure. The reflected wave induces currents in the TEM feed arm, which can radiate again. An example path for this signal is drawn and marked by **P**. The wave reflected from the edge of the reflector also radiates. This is marked by **E**. For the flat IRA, signal **E** also includes the signal taking multiple-reflection path, e.g., drive point – reflector – TEM feed arm – reflector – observer. The signal taking this path appears at $t_r/\tau_a \simeq 2$ for the tall IRA. The multiple reflection paths are longer so the peaks in the tail waveforms are more spread

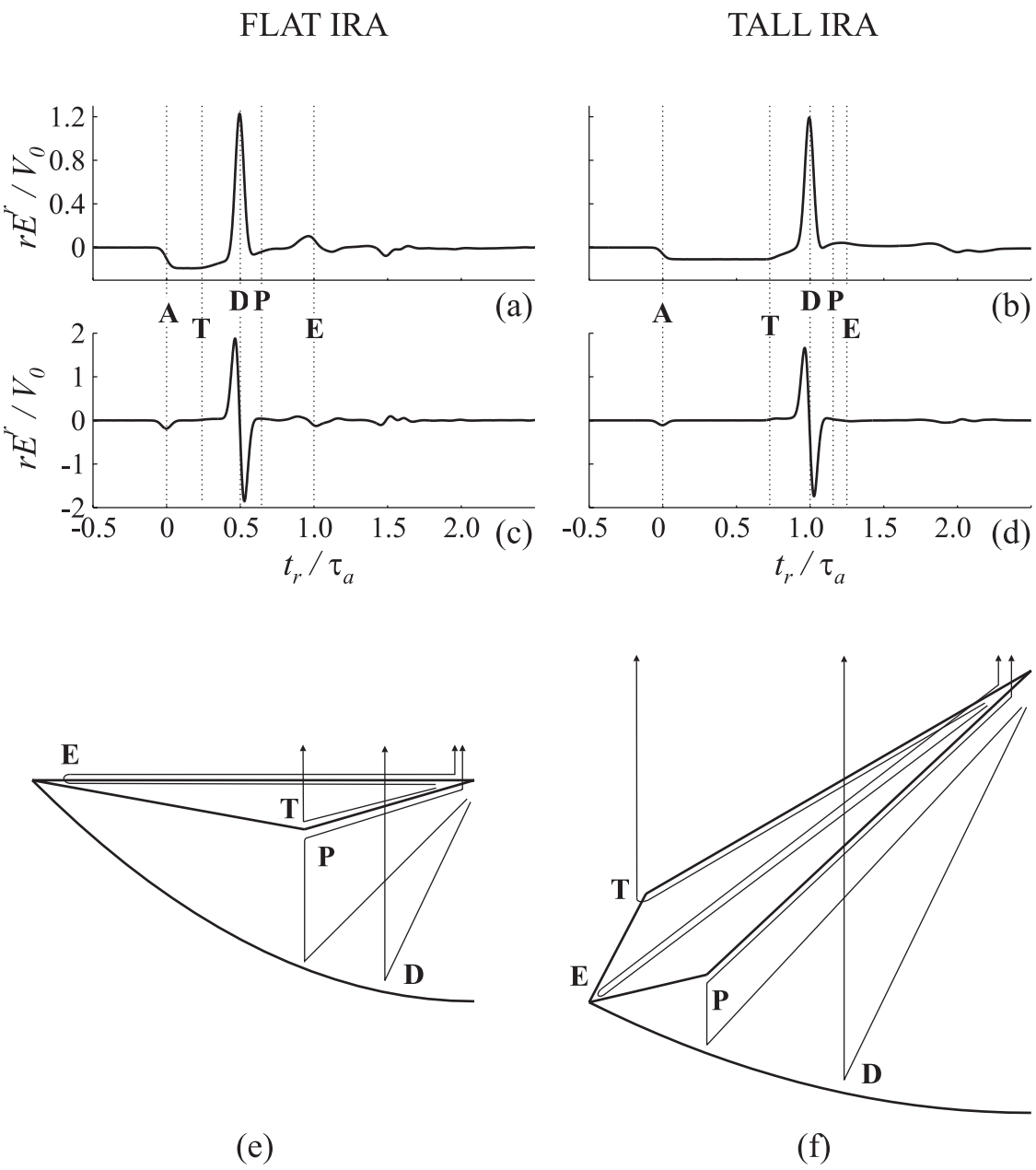

Fig. 10. Analysis of the radiated waveforms. (a), (b) Radiated waveforms when the input pulse is a step-like with $t_{10\text{-}90\%}/\tau_a = 0.075$. (c), (d) Radiated waveforms when the input pulse is a Gaussian with $t_{FWHM}/\tau_a = 0.075$. (e), (f) Wave and current paths.

out for the tall IRA than the flat IRA.

Because the prepulse is a replica of the signal at the drive point, the prepulse amplitude does not depend strongly on the input pulse rise time. However, the impulse amplitude depends on the pulse rise time because the waveform is a derivative of the drive point signal. Fig. 11 shows the variation of the radiated waveforms according to the input pulse parameters. The radiated fields are graphed as functions of time for step-like, Gaussian, and differentiated Gaussian pulses and vertically shifted according to the pulse parameters. The input pulse waveforms are shown in the left column. The prepulse amplitude does not vary much according to the input pulse. In fact, the prepulse amplitude is constant for fast rising pulses irrespective of the pulse parameter. However, the impulse amplitude strongly depends on the input pulse. For fast rising pulses, the impulse is large in amplitude and short in duration because the impulse waveform is a derivative of the input pulse. For slowly rising pulses, the impulse is small and long. The long impulse eats into the prepulse. For an IRA with a small F/D, the impulse eats into the prepulse before the prepulse reaches its theoretical maximum and therefore lowers the prepulse amplitude. This can be easily seen in Fig. 11 (b) for $t_{10\text{-}90\%}/\tau_a \leq 0.2$.

Fig. 12 shows the radiated fields of the two IRAs at a number of observation angles around the boresight direction. The input pulses for this figure are a step-like pulse with $t_{10\text{-}90\%}/\tau_a = 0.075$ and a Gaussian pulse with $t_{FWHM}/\tau_a = 0.075$. The angles are measured in the y-z plane (E-plane) and in the x-z plane (H-plane) from the rotational axis of the reflector. The impulse is lowered and distorted rapidly with increasing observation angle because the aperture field is focused at $\theta = 0$. However, the shape and amplitude of the prepulse vary slowly with respect to the observation angle.

The impulse and prepulse amplitudes are summarized in Fig. 13 as functions of observation angle for a range of step-like pulses. The lines in the left hand side of each graph represent the impulse and prepulse amplitudes in the H-plane, and the lines in the right hand side of each graph represent those in the E-plane. Because the distinction between the impulse and prepulse is obscure off boresight, simply the maximum and minimum of the radiated field (rE^r/V_0) are taken as the impulse and prepulse amplitudes, respectively.

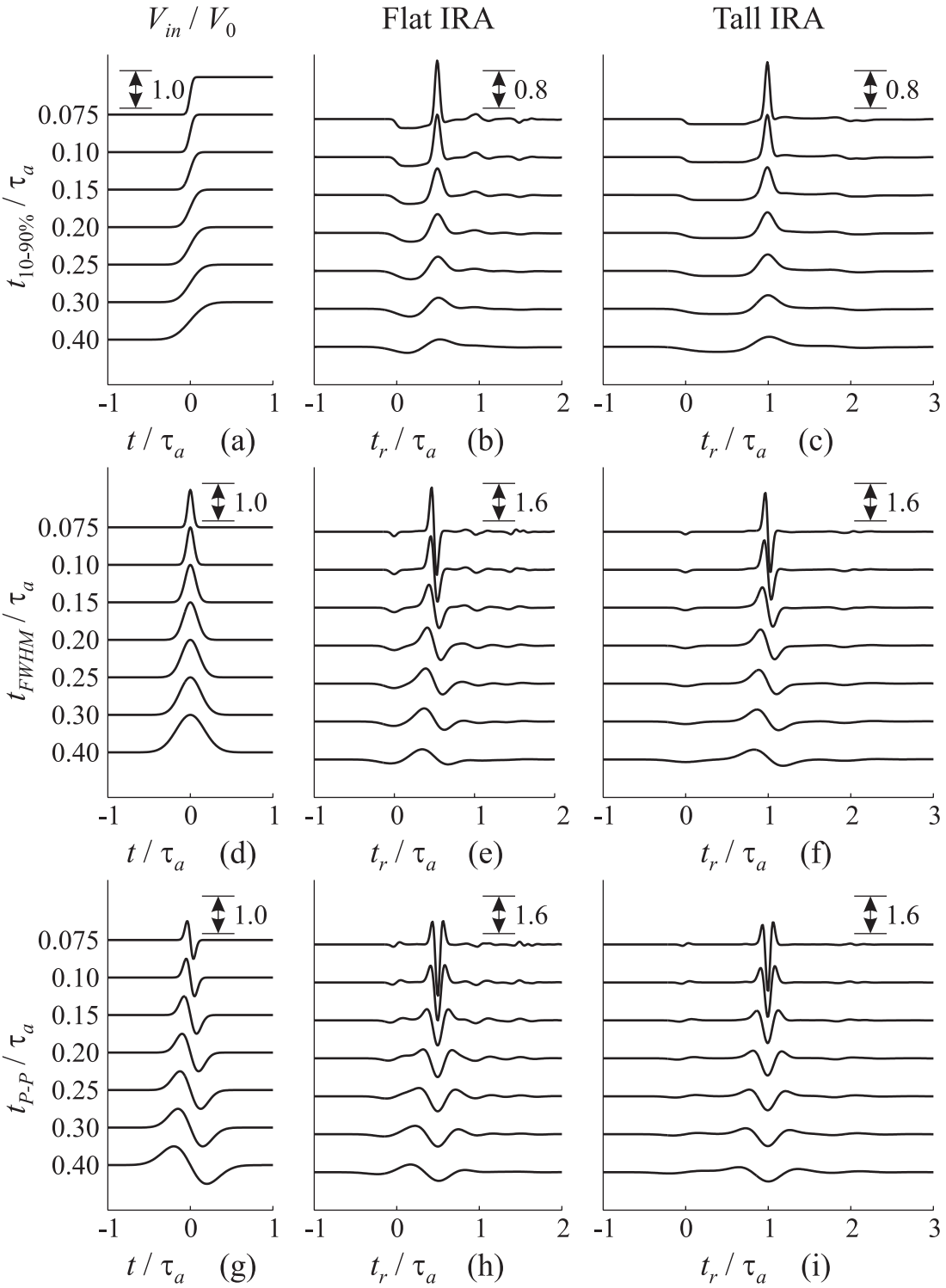

Fig. 11. Radiated fields (rE^r/V_0) on boresight as functions of time for a range of input pulse parameters. (a), (d), (g) Waveforms of step-like, Gaussian, and differentiated Gaussian pulses. (b), (e), (h) Radiated fields from the flat IRA. (c), (f), (i) Radiated fields from the tall IRA.

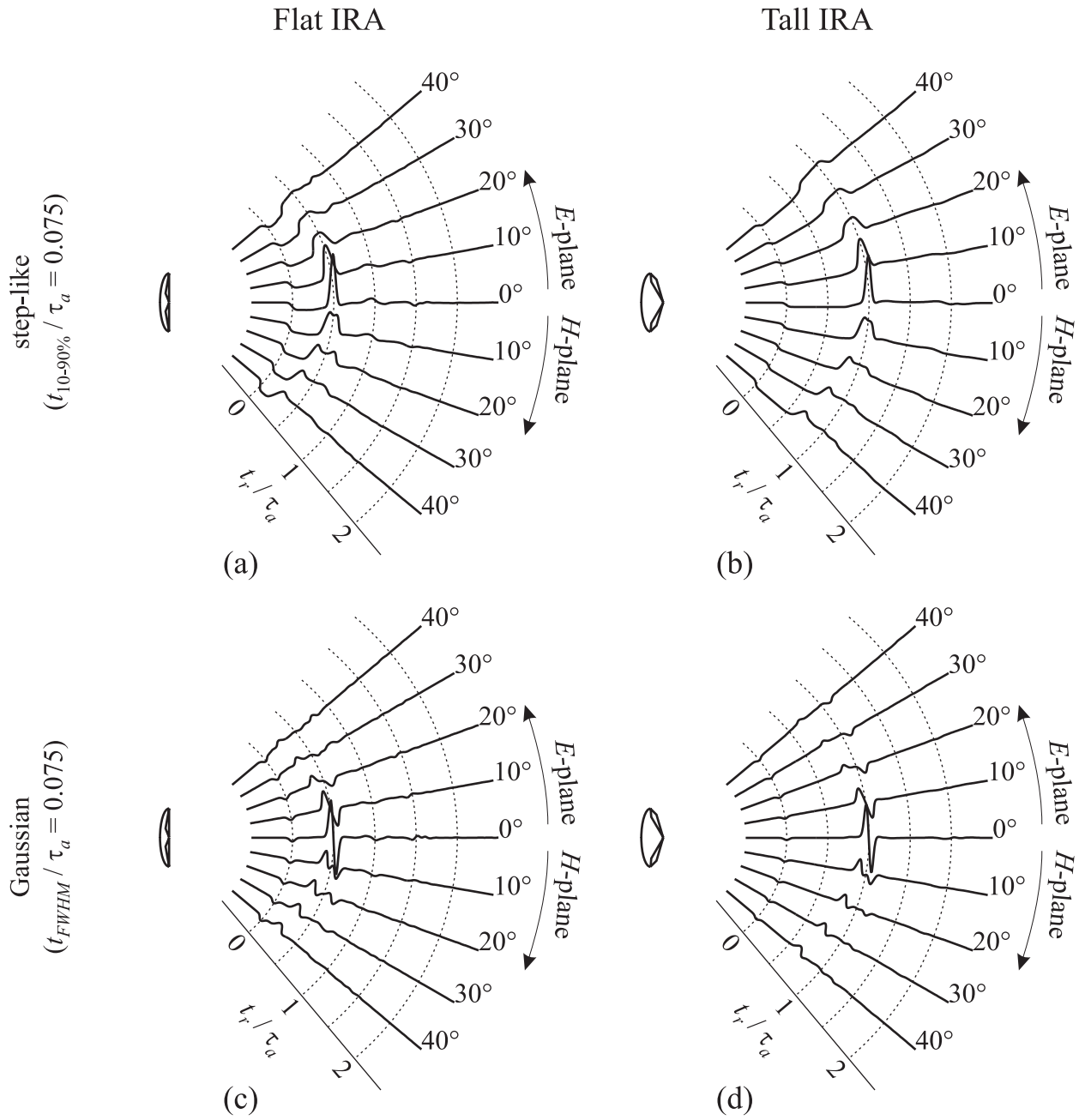

Fig. 12. Radiated fields at a number of observation angles. Input pulses are (a), (b) a step-like pulse with $t_{10\text{-}90\%}/\tau_a = 0.075$ and (c), (d) a Gaussian pulse with $t_{FWHM}/\tau_a = 0.075$.

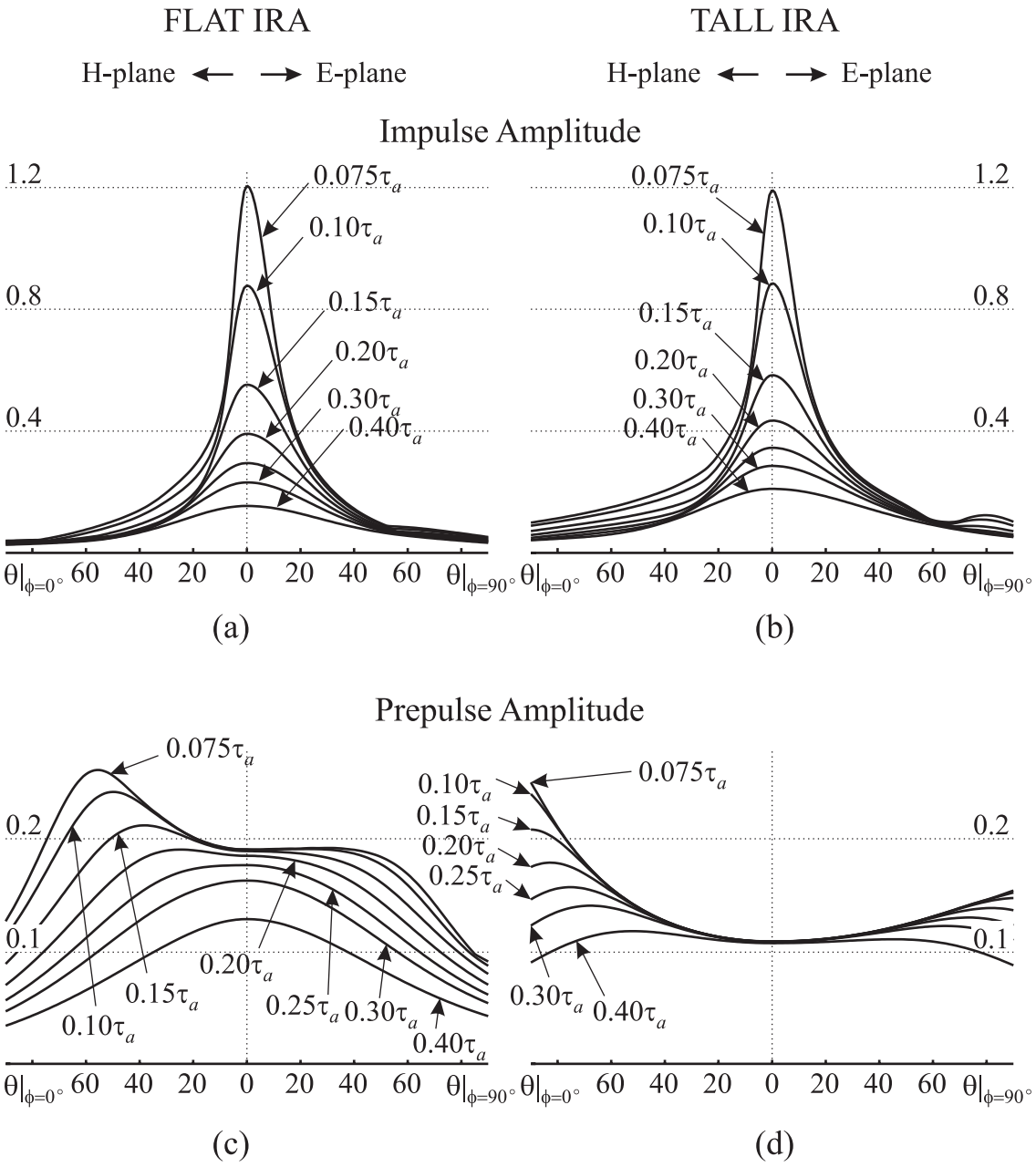

Fig. 13. Amplitudes of the impulse and prepulse as functions of observation angle. (a), (b) Impulse amplitudes ($\max rE^r/V_0$). (c), (d) Prepulse amplitudes ($\min rE^r/V_0$).

The impulse amplitude at small angles increases rapidly with decreasing pulse rise time, which is expected from the simple analytical model. For fast rising pulses, the impulse is large at small angles and decreases rapidly with increasing observation angle. The half-maximum (θ_{HM}) angle, which is the observation angle where the amplitude drops by half from its maximum, decreases with decreasing pulse rise time. Thus, the impulse is strong only in a narrow angle. The figure shows that θ_{HM} is smaller in the H-plane than in the E-plane.

The prepulse amplitude remains constant at small angles and depends strongly on the pulse rise time at large angles. However, in Fig. 13 (c), the prepulse for the flat IRA at small angles decreases with increasing pulse rise time for $t_{10\text{-}90\%}/\tau_a \geq 0.2$. The reason for this is that the prepulse and impulse overlap and lower each other when the input pulse rises slowly. The decrease in the impulse amplitude on boresight for slowly rising pulses is seen in Fig. 13 (a). This effect is not seen in Fig. 13 (b), (d) for the tall IRA because its prepulse is longer in duration. This effect will occur with a pulse rise time larger than $t_{10\text{-}90\%}/\tau_a \simeq 0.4$.

Next, Fig. 14 shows the radiated fields (E_y) on the rotational axis of the reflector at distances close to the antenna. The input pulses for this figure are a step-like with $t_{10\text{-}90\%}/\tau_a = 0.075$, a Gaussian with $t_{FWHM}/\tau_a = 0.075$, and a differentiated Gaussian with $t_{P\text{-}P}/\tau_a = 0.075$. In each graph, the radiated field is normalized by V_0/r and vertically displaced according to the observation distance. The figure shows that the prepulse stays constant because it originates at one point (drive point) and propagates spherically. The impulse varies according to the observation distance. For a step-like pulse, the impulse is small in amplitude and long in duration at distances close to the antenna. The impulse becomes large in amplitude and short in duration as the observer moves farther away because the impulse is the radiation from the aperture field focused at infinity.

Fig. 15 shows the normalized impulse amplitude ($\max rE_y/V_0$) on boresight as a function of the observation distance for a range of step-like pulses. The figure shows that the normalized amplitude increases rapidly with increasing observation distance at distances close to the antenna and converges slowly to the far-field amplitude at distances far from the antenna. Also note that the impulse amplitude is larger for a smaller pulse rise time at

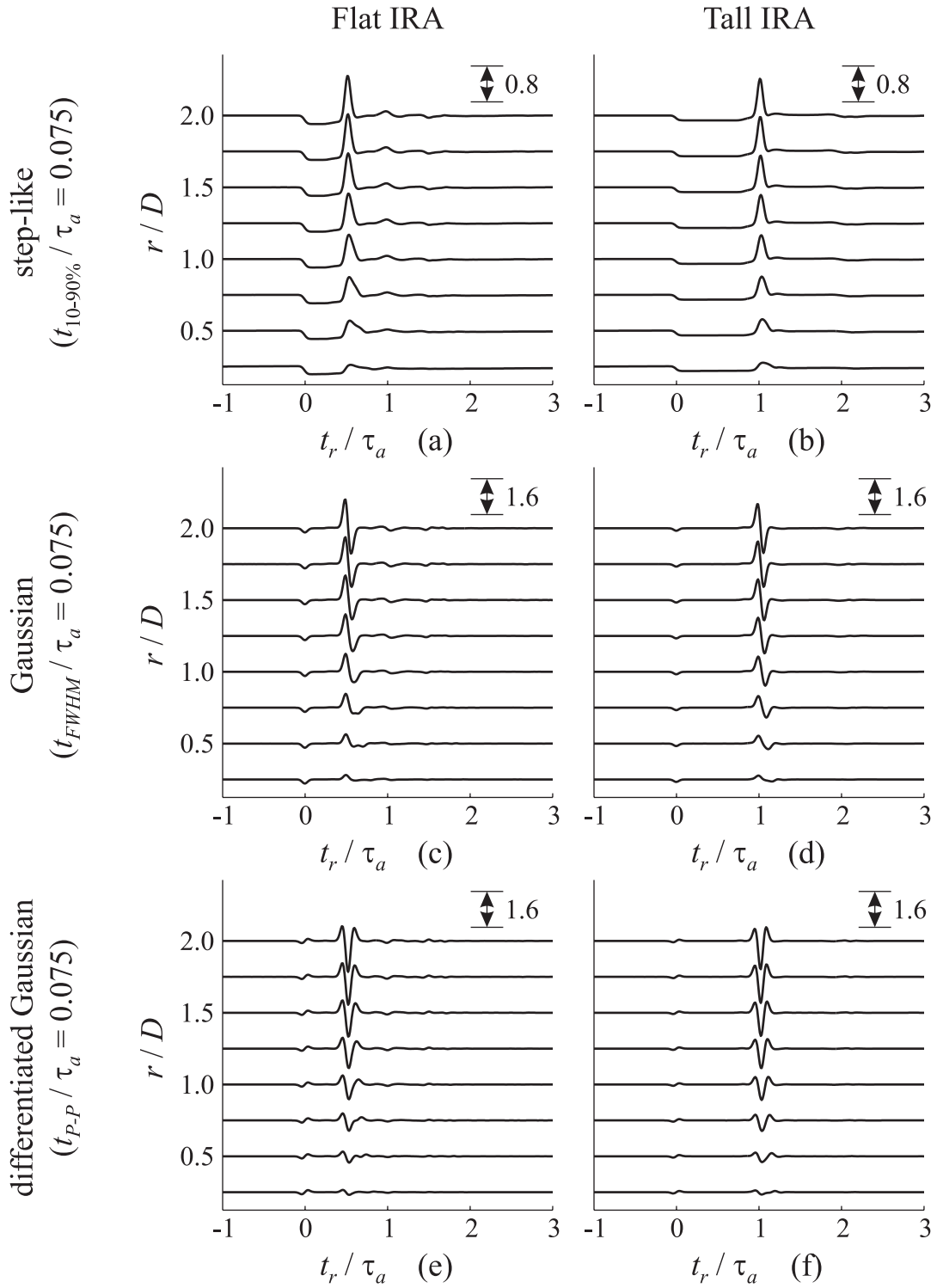

Fig. 14. Graphs of the normalized electric field (rE_y/V_0) on boresight as a function of time at a number of observation distances. The input pulses are (a), (b) a step-like with $t_{10\text{-}90\%}/\tau_a = 0.075$, (c), (d) a Gaussian with $t_{FWHM}/\tau_a = 0.075$, and (e), (f) a differentiated Gaussian with $t_{P\text{-}P}/\tau_a = 0.075$.

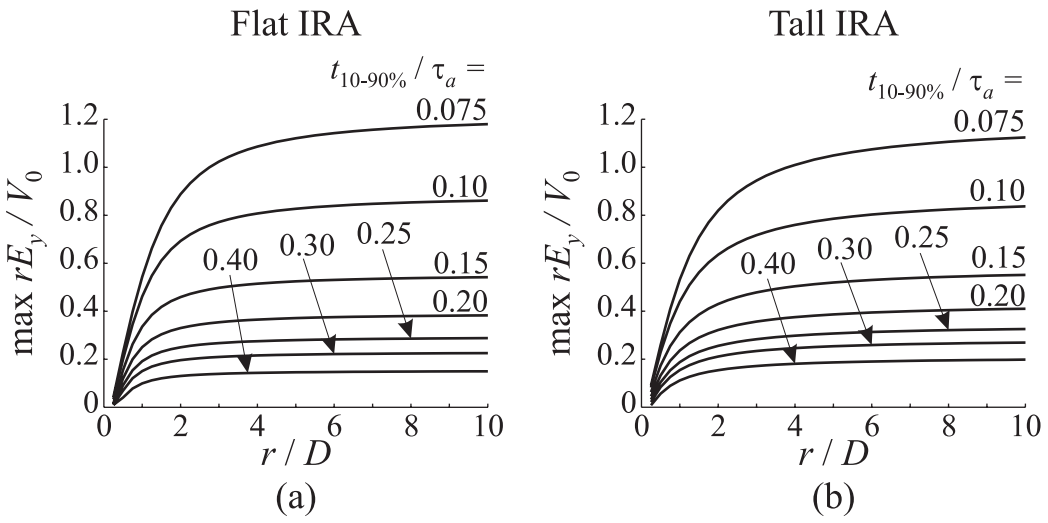

Fig. 15. Impulse amplitudes (rE_y/V_0) for (a) the flat IRA and (b) the tall IRA as functions of observation distance for a number of step-like pulses.

all points.

Fig. 13 showed that the impulse in the far-field is strong only in a narrow angle for a fast rising step-like pulse. This can be shown in terms of the spot size at distances close to the antenna. To determine a spot size, an imaginary observation plane that is normal to the rotational axis of the reflector is placed at a distance, where the impulse amplitude (maximum of E_y) distribution is recorded. Then the half-maximum width of the distribution is taken as the spot size. Fig. 16 compares the spot sizes of the flat IRA and the tall IRA as functions of observation distance for a number of step-like pulses. The lines above the horizontal axis represent the spot sizes measured in the E-plane, and the lines below the horizontal axis represent those measured in the H-plane. The figure shows that the spot size decreases with decreasing pulse rise time, and therefore the impulse beam width decreases with decreasing pulse rise time. Note that the spot size is smaller in the H-plane than in the E-plane for both antennas. Also, the spot size is smaller for the flat IRA than for the tall IRA.

Next, we will analyze the reflected voltage in the transmission line when the antenna is radiating in free space. In Fig. 17, the reflected voltages in the transmission line are plotted for a step-like pulse with $t_{10\text{-}90\%}/\tau_a = 0.075$ and a Gaussian pulse with $t_{FWHM}/\tau_a = 0.075$. For each antenna, the first signal **A** centered at $t/\tau_a \simeq 0$ is the reflection from the drive point.

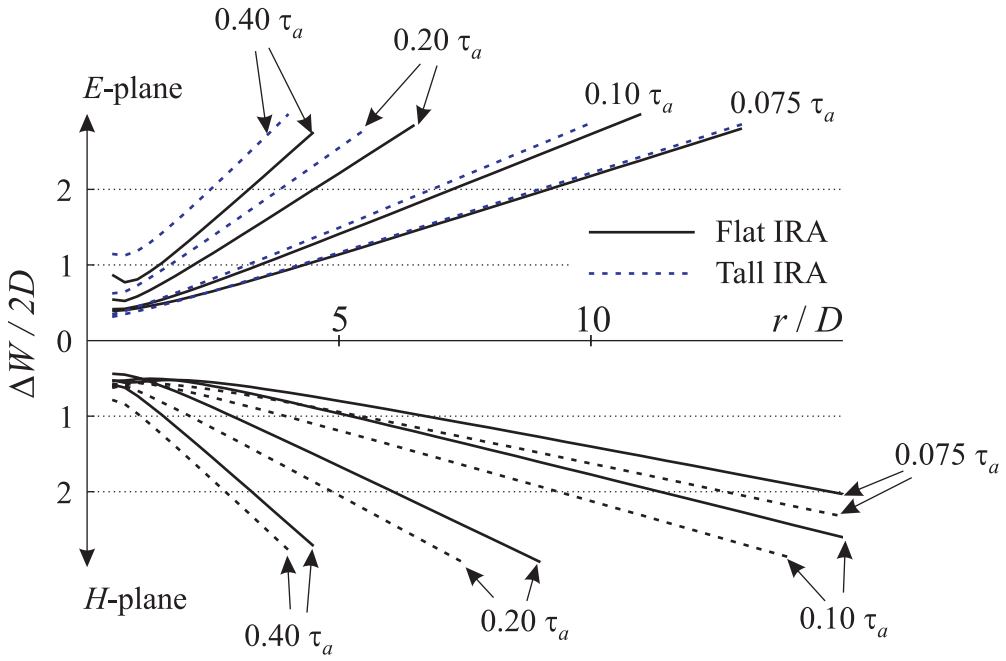

Fig. 16. Spot sizes of the flat IRA (solid lines) and the tall IRA (dotted lines) for a number of step-like pulses. The lines above the horizontal axis represent half spot sizes ($\Delta W/2$) in the E-plane, and the lines below the horizontal axis represent those in the H-plane. The spot sizes are normalized by the reflector diameter (D).

The beginning of the signal from the tapered section of the TEM feed arms is marked by **T**. Because the amount of metal gradually decreases along the taper, the impedance of the TEM feed arms gradually increases, and therefore the wave is continuously and positively reflected until the wave reaches the resistor. When the wave reaches the resistor, the wave experiences a sudden drop in the impedance (200Ω resistor and metal reflector), and is reflected negatively (**E**). Meanwhile, the wave propagating toward the reflector is negatively reflected at the reflector surface. The reflected wave induces currents along the arms. **D** and **P** show two of these wave paths. Note that **D** is observed earlier than **P** because of the difference in the wave path lengths. Note also that the waveform for the flat IRA is more complicated than that for the tall IRA because the signals (**T**, **D**, **P**, and **E**) for the flat IRA are more spread out in time than those for the tall IRA.

Fig. 18 shows the variation in the reflected voltage waveforms caused by the change in the input pulse parameter. Note the interesting behavior of the waveforms of the tall IRA at $t/\tau_a \simeq 1.3$. In Fig. 18 (c), the amplitude of the waveform increases with decreasing

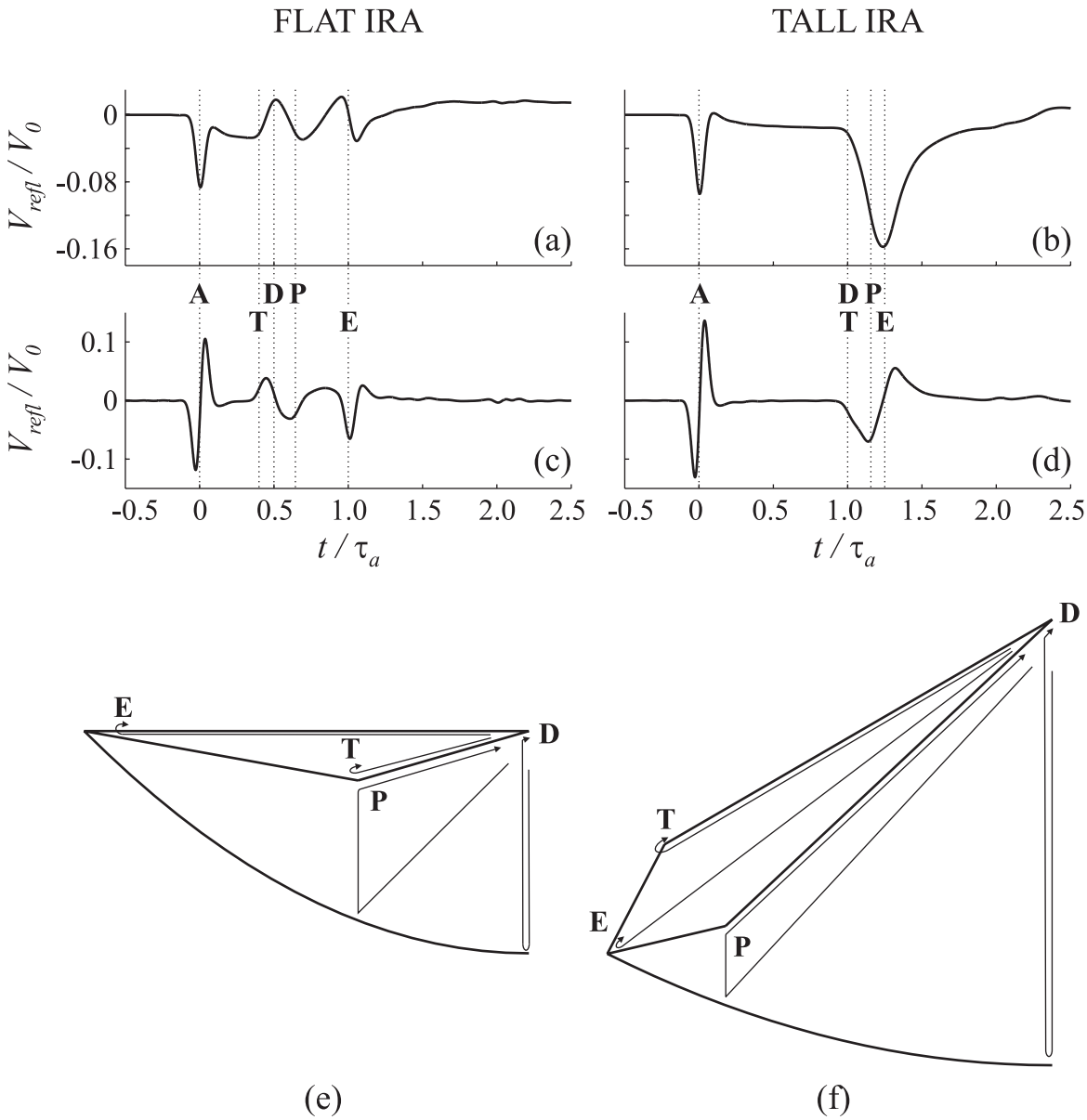

Fig. 17. Analysis of the reflected voltages in the transmission line. (a), (b) Reflected voltages when the input pulse is a step-like with $t_{10\text{-}90\%}/\tau_a = 0.075$. (c), (d) Reflected voltages when the input pulse is a Gaussian with $t_{FWHM}/\tau_a = 0.075$. (e), (f) Wave and current paths.

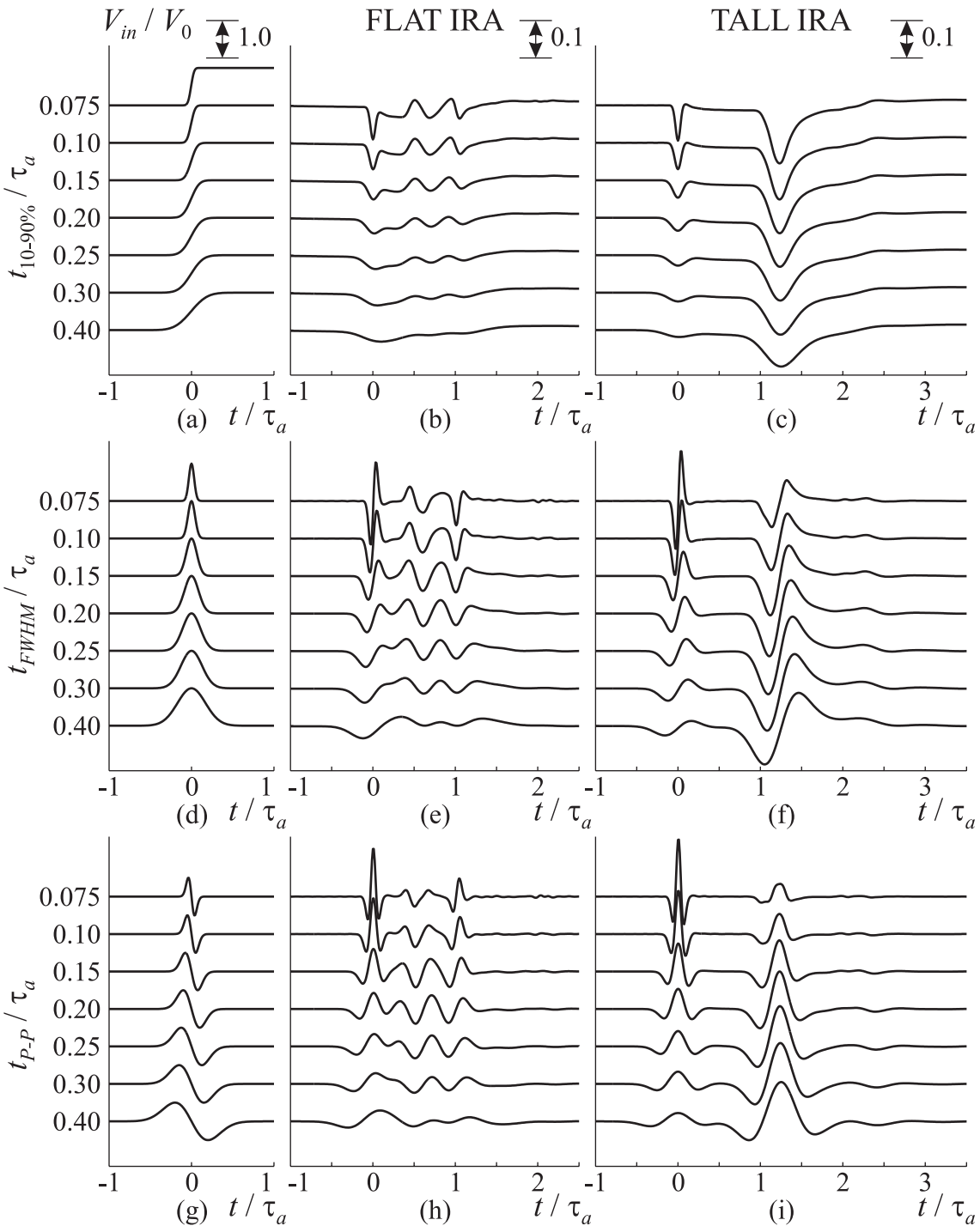

Fig. 18. Reflected voltages in the transmission line as functions of time for a range of pulse parameters. (a), (d), (g) Waveforms of step-like, Gaussian, and differentiated Gaussian pulses. (b), (e), (h) Reflected voltages (V_{refl}/V_0) from the flat IRA for the input pulses. (c), (f), (i) Reflected voltages from the tall IRA for the input pulses. Note that the vertical scale for the input pulse waveforms is 1.0, and the vertical scale for the reflected voltages is 0.1.

pulse parameter, $t_{10\text{-}90\%}$, but in Fig. 18 (f), (i), the amplitude of the waveform decreases with decreasing pulse parameters in the ranges of $t_{FWHM}/\tau_a < 0.3$ and $t_{P\text{-}P}/\tau_a < 0.3$. The reason for this behavior is that, in the low frequency range, the reflection coefficient of the tall IRA results in the maximum response in the time domain for the pulses with $t_{FWHM}/\tau_a \simeq 0.3$ and $t_{P\text{-}P}/\tau_a \simeq 0.3$.

Finally, in Fig. 19, the power budgets for the two IRAs are shown. The power reflected back in the transmission line (P_{refl}), the power dissipated in the matching circuits (P_{diss}), and the power radiated in free space (P_{rad}) are shown as functions of normalized frequency. The powers are normalized by the incident power in the transmission line (P_{in}). For both IRAs, the reflected power is small over the entire frequency range, and therefore the IRA is well matched to the 200Ω transmission line. At low frequencies, the power dissipated in the matching circuits is larger than the power radiated. However, at high frequencies, the radiated power is larger than the dissipated power. The radiated power increases with increasing frequency and reaches almost unity at the highest frequency. This indicates that the radiation efficiency of the IRA increases with increasing frequency. Note the frequency where the radiated power begins to exceed the dissipated power. This frequency is lower for the tall IRA than the flat IRA, and therefore the radiation efficiency of the tall IRA is higher than that of the flat IRA at low frequencies. The reason for this is that the tall IRA has a longer focal length than the flat IRA. This allows both the impulse and the prepulse to radiate better for a slowly rising pulse, whose frequency content is low.

V. Conclusion

A numerical model using EIGER was developed for the IRA. The model was made efficient by eliminating geometrical redundancies. Only half of the reflector and one TEM feed arm were meshed. The performance of the numerical model was validated by comparing the radiated field measured on boresight and the reflected voltage measured in the transmission line with the results from the numerical model.

The IRAs with $F/D = 0.25$ and 0.5 were analyzed. The radiated waveform predicted

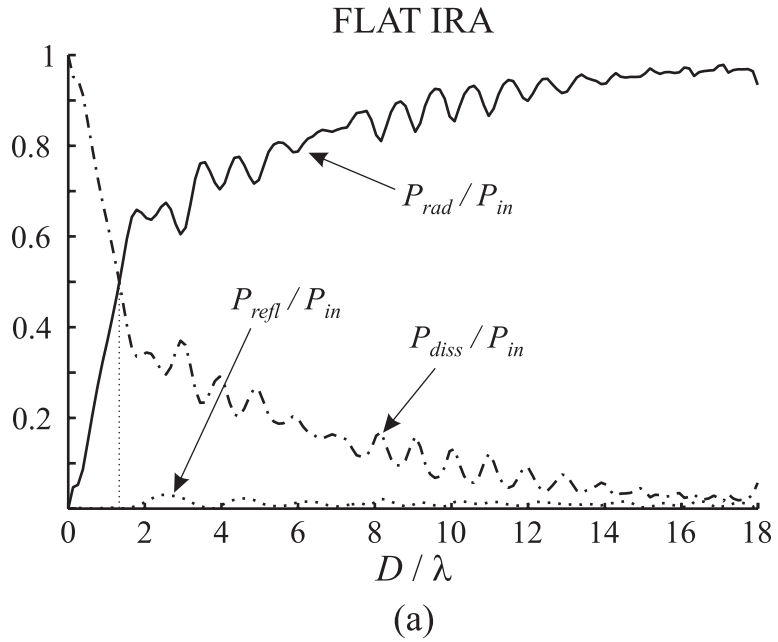

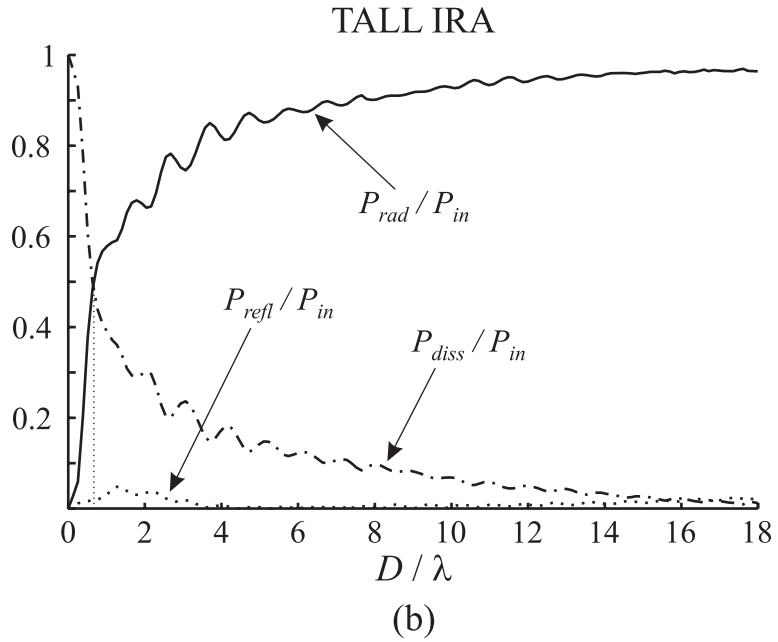

Fig. 19. Power budgets of (a) the flat IRA and (b) the tall IRA as functions of normalized frequency (D/λ). The powers are normalized by the power incident in the transmission line.

by the numerical model was compared with the one predicted by the simple analytical model. They were different mostly in the prepulse and tail waveforms. By conducting a simple wave path analysis, the causes of the differences were identified. The prepulse was distorted near the impulse because of the disturbance in the TEM feed arm taper. The postpulses were due to the multiple reflections inside the antenna, and therefore they were more spread out for the IRA with a larger F/D.

The radiated waveform on boresight was plotted for step-like, Gaussian, and differentiated Gaussian pulses for a range of pulse-parameters. The impulse amplitude depended strongly on the input pulse parameter because the impulse was a derivative of the input pulse. The prepulse amplitude did not depend strongly on the input pulse parameter for fast rising pulses. However for slowly rising pulses, the prepulse was seen to be lowered because the prepulse and the impulse overlap and lower each other. Because the prepulse of the flat IRA is shorter than that of the tall IRA, the flat IRA suffers more from this phenomenon.

The radiated waveform was also plotted for a number of observation angles for a step-like and a Gaussian pulses. The amplitude and shape of the prepulse did not depend strongly on the observation angle. However, the shape of the impulse was distorted rapidly with increasing observation angle. The summary graph was drawn for the impulse and prepulse amplitudes for a range of step-like pulses at a number of observation angles. The graph showed that the impulse was directive in the far-zone. This directive property was also shown at distances close to the antenna by plotting the illuminated spot sizes.

The normalized electric fields at distances close to the antenna were plotted for the three types of input pulses. The prepulse stayed constant because it originated at one point (drive point) and propagated spherically. The impulse was small in amplitude and long in duration at distances close to the antenna. The impulse became large in amplitude and short in duration as the observer moves farther away because the impulse is the radiation from the aperture field focused at infinity. The summary graph for the impulse amplitude was presented as a function of observation distance for a range of step-like pulses.

A simple wave path analysis was conducted for the signals in the reflected voltage in

the transmission line, and the origins of the signals were identified. Also, the reflected voltage in the transmission line was plotted for step-like, Gaussian, and differentiated Gaussian pulses for a range of pulse-parameters. The voltage waveform for the flat IRA was complicated. However, the voltage waveform for the tall IRA was simple because the signals were spaced closely so they were not independently distinguishable.

Finally, the power budget analysis was conducted, and it showed that the radiation efficiency at low frequency was higher for the IRA with a larger F/D than for the IRA with a smaller F/D because the prepulse and postpulses overlap less for the IRAs with a larger F/D.

VI. Acknowledgement

This work is supported in part by the US Army CECOM RDEC Night Vision and Electronic Sensors Directorate, Countermine Division.

References

1. G. Sower, J. Eberly, and E. Christy, "GSTAMIDS ground-penetrating radar: hardware description," in *Detection and Remediation Technologies for Mines and Minelike Targets VI, Proc. SPIE*, vol. 4394, Apr. 2001, pp. 651–661.

2. E. G. Farr, "Analysis of the impulse radiating antenna," C. E. Baum, Ed. Albuquerque, NM: USAF Philiips Lab, July 24, 1991, Sensor and Simulation Notes #329.

3. T. P. Montoya, "Vee dipole antennas for use in short-pulse ground-penetrating radars," Ph.D. dissertation, Georgia Institute of Technology, Mar. 1998.

4. E. G. Farr and L. H. Bowen, "Impulse radiating antennas for mine detection," in *Detection and Remediation Technologies for Mines and Minelike Targets VI, Proc. SPIE*, vol. 4394, Apr. 2001, pp. 680–691.

5. J. R. R. Pressley, D. Pabst, G. Sower, L. Nee, B. Green, and P. Howard, "Ground standoff mine detection system (GSTAMIDS) engineering, manufacturing and development (EMD) block 0," in *Detection and Remediation Technologies for Mines and Minelike Targets VI, Proc. SPIE*, vol. 4394, Apr. 2001, pp. 1190–1200.

6. D. V. Giri, H. Lackner, I. D. Smith, D. W. Morton, C. E. Baum, J. R. Marek, W. D. Prather, and D. W. Scholfield, "Design, fabrication, and testing of a paraboloidal reflector antenna and pulser system for impulse-like waveforms," *IEEE Trans. Plasma Sci.*, vol. 25, no. 2, pp. 318–326, Apr. 1997.

7. C. E. Baum, E. G. Farr, and D. V. Giri, "Review of impulse-radiating antennas," in *Reviw of Radio Science 1996-1999*. W. R. Stone, Ed. Oxford University Press, 1999, ch. 16, pp. 403–439.

8. C. E. Baum, "Radiation of impulse-like transient fields," C. E. Baum, Ed. Albuquerque, NM: USAF Philiips Lab, Nov. 25, 1989, Sensor and Simulation Notes #321.

9. C. E. Baum and E. G. Farr, "Impulse radiating antennas," in *Ultra-Wideband, Short Pulse Electromagnetics*. H. Bertoni *et al.,* Eds. New York: Plenum, 1993, pp. 139–147.

10. E. G. Farr, C. E. Baum, and C. J. Buchenauer, "Impulse radiating antennas, part II," in *Ultra-Wideband, Short Pulse Electromagnetics 2*. L. Carin and L. B. Felsen, Eds. New York: Plenum, 1995, pp. 159–170.

11. E. G. Farr and C. E. Baum, "Prepulse associated with the TEM feed of an impulse radiating antenna," C. E. Baum, Ed. Albuquerque, NM: USAF Phillips Lab, Mar. 1992, Sensor and Simulation Notes #337.

12. ——, "The radiation pattern of reflector impulse radiating antennas: Early-time response," C. E. Baum, Ed. Albuquerque, NM: USAF Philiips Lab, Jun. 1993, Sensor

and Simulation Notes #358.

13. C. E. Baum, "Intermediate field of an impulse-radiating antenna," C. E. Baum, Ed. Albuquerque, NM: USAF Phillips Lab, Dec. 22, 1997, Sensor and Simulation Notes #418.

14. O. V. Mikheev, S. A. Podosenov, K. Y. Sakharov, A. A. Sokolov, Y. G. Svekis, and V. A. Turkin, "New method for calculating pulse radiation from an antenna with a reflector," *IEEE Trans. Electromagn. Compat.*, vol. 39, no. 1, pp. 48–54, Feb. 1997.

15. R. M. Sharpe, J. B. Grant, N. J. Champagne, W. A. Johnson, R. E. Jorgenson, D. R. Wilton, W. J. Brown, and J. W. Rockway, "EIGER: Electromagnetic interactions generalized," in *IEEE AP-S Int'l Symp. Digest, Quebec, Canada*, Jul. 1997, pp. 2366–2369.

16. Lawrence Livermore National Laboratory. (2001, March 5) EIGER - A Revolution in Computational Electromagnetics. [Online]. Available: http://cce.llnl.gov/eiger/

17. ——. (2002, Sept. 24) EIGER User's Guide. [Online]. Available: http://cce.llnl.gov/eiger

18. C. E. Baum, "Configuration of TEM feed for an IRA," C. E. Baum, Ed. Albuquerque, NM: USAF Philiips Lab, Apr. 27, 1991, Sensor and Simulation Notes #327.

19. N. J. Champagne. (2001, March 5) EIGER FAQ. [Online]. Available: http://cce.llnl.gov/eiger/support/eiger_faq.html

20. K. Kim, "Numerical and experimental investigation of impulse-radiating antennas for use in sensing applications," Ph.D. dissertation, Georgia Institute of Technology, April 2003.

21. M. Abramowitz and I. A. Stegun, *Handbook of Mathematical Functions with Formulas, Graphs, and Mathematical Tables.* New York: Dover, 1972.

22. Picosecond Pulse Labs (2001, May 5), "Model 5315A Balun, Differential Pulse Splitter Specification Sheet," [Online]. Avaliable: http://www.picosecond.com.

23. D. M. Pozar, *Microwave Engineering*, 2nd ed. New York: John Wiley & Sons, Inc., 1998.

24. E. G. Farr, "Optimizing the feed impedance of impulse radiating antennas, Part I: Reflector IRAs," C. E. Baum, Ed. Albuquerque, NM: USAF Philiips Lab, Jan. 1993, Sensor and Simulation Notes #354.